

Comprehensive assessment of five global daily downward shortwave radiation satellite products

Ruohan Li, Dongdong Wang*, Shunlin Liang

Department of Geographical Sciences, University of Maryland, College Park, MD, 20742, USA



ARTICLE INFO

Keywords:

Downward shortwave radiation
Satellite products validation
High latitude
High spatial resolution

ABSTRACT

The downward shortwave radiation (DSR) is a critical parameter of the surface radiation budget. Several DSR satellite products have been developed in recent years. In this study, five updated global satellite daily DSR products were evaluated using *in situ* measurements from 142 global sites with a special focus on high latitudes in 2004. These five products are Clouds and the Earth's Radiant Energy System Synoptic TOA and surface fluxes and clouds (CERES), Clouds, Albedo and Radiation Edition 2 data (CLARA), Global Land Surface Satellite Downward Shortwave Radiation (GLASS), Breathing Earth System Simulator (BESS) shortwave radiation product, and Moderate Resolution Imaging Spectroradiometer land surface Downward Shortwave Radiation (MCD18) with a spatial resolution of 100, 25, 5, 5, and 1 km, respectively. The CERES, BESS, and MCD18 provide full global coverage throughout the year, whereas CLARA and GLASS present different levels of seasonal data loss over high-latitude areas. The products were aggregated and compared at various spatial resolutions over different subareas. The overall accuracy increased after the products were aggregated to 100 km. However, the highest accuracy was achieved at a resolution of 25 km over high-latitude areas for GLASS and MCD18. When all products were evaluated at a resolution of 100 km, the global root-mean-square error of CERES, CLARA, GLASS, BESS, and MCD18 was 27.6, 29.1, 30.3, 29.6, and 31.6 W/m², respectively, and the mean bias difference was 2.2, -1.5, -1.8, -3.4, and -8.0 W/m². The accuracies of most products are ~7 W/m² lower over high-latitude areas. A seasonal variation of the accuracies was observed for all products. It is particularly pronounced over high-latitude areas. With respect to the long term, both *in situ* data, BESS, and CERES show insignificant trends, while CLARA and GLASS present dimming trend. Besides, CLARA and GLASS exhibit slight annual changes of -0.250 and -0.387 W/m² in the bias and 0.357 and 0.310 Wm⁻² in the RMSE in the past two decades. GLASS and MCD18 exhibit a superior performance over coastal regions but degrade over snow-covered areas. Potential refinements of current high-resolution DSR retrieval algorithms are suggested, which will improve the retrieval accuracy. Highly accurate products with a long-term stability, especially over high-latitude areas, are required for future climate change analyses.

1. Introduction

Surface downward shortwave radiation (DSR) is a critical component of the surface energy and radiation budget. It is also a fundamental driving force of many hydrological, ecological, and biogeochemical surface processes (Liang et al., 2010, 2019). The DSR promotes the exchange of water, energy, carbon, and other agents among the land surface, atmosphere, and oceans and thus is of particular importance for modeling various land surface processes (Huang et al., 2019; Liang et al., 2010; Stephens et al., 2012). With the rapid development of solar energy technologies and the increasing demand for renewable and clean

energy, it is necessary to precisely estimate the incident solar energy to plan and manage solar power plants (Gueymard, 2014; Jiang et al., 2019).

The results of previous studies demonstrated that satellite data could be used to estimate the DSR. Retrieval methods can be generally divided into two categories. The first type of method is based on physical models, that is, mainly radiative transfer models (RTM) at the surface, top-of-the-atmosphere (TOA), and within the atmosphere (Urraca et al., 2017). The core idea of this type of method is to improve the computational efficiency of the RTM, leading to further methods such as parameterization and simplified look-up-table (LUT)-based methods

* Corresponding author. Department of Geographical Sciences, University of Maryland, 1127 LeFrak Hall, College Park, MD, 20742, USA.
E-mail address: ddwang@umd.edu (D. Wang).

(Huang et al., 2019). Statistical models represent the second category. They are based on the empirical relationship between satellite observations and atmospheric and surface parameters (Huang et al., 2019; Urraca et al., 2017). Examples of these methods include recent studies in which machine learning techniques were employed to estimate the DSR (Brown et al., 2020; Wang et al., 2012).

Many satellite DSR products have been generated by applying the above-mentioned methods. Several global products are based on polar-orbiting satellite data or their combination with geostationary data such as the Clouds and the Earth's Radiant Energy System (CERES; Kato et al., 2013), Global Energy and Water Cycle Experiment - Surface Radiation Budget (GEWEX/SRB; Pinker and Laszlo, 1992), and International Satellite Cloud Climatology Project -Flux Data (ISCCP-FD; Yuanchong Zhang et al., 2004). In addition, several regional products have been generated from geostationary satellites such as Himawari-8 (Yu et al., 2018), METEOSAT Second Generation (Pfeifroth et al., 2018), and Goddard Earth Observing System (GEOS).

Many DSR validations and assessments have been conducted (Boilley and Wald, 2015; Gui et al., 2010; Jia et al., 2013; Pfeifroth et al., 2018; Posselt et al., 2012; Sanchez-Lorenzo et al., 2015; Sun et al., 2018; Urraca et al., 2017; Wu and Fu, 2011; Xia et al., 2006; Yu et al., 2018; 2019; Zhang et al., 2015; 2016). However, most of them were focused on regional areas such as Europe or East Asia. With respect to global analysis, the polar region has rarely been thoroughly investigated because of the limited availability of field measurement stations over high-latitude areas. However, the shortwave radiation over high-latitude areas is extremely important for studies of global climate change due to the polar region's unique location and weather characteristics (Sun et al., 2018). It influences the variability of the polar climate and ecological environment by directly or indirectly affecting snow melt and refreezing, the sea ice extent, surface albedo, and oceanic circulation (Kapsch et al., 2016; Yehui Zhang et al., 2011). In addition, it is difficult to accurately estimate the DSR by satellites because of the low solar incident angle and high snow coverage over high-latitude areas and thus comprehensive analyses are needed.

Previous global assessments were mostly based on CERES, GEWEX/SRB, ISCCP-FD, or reanalysis data such as ERA-Interim (Gui et al., 2010; Zhang et al., 2013; 2015). However, several of these products have not been updated since the 2000s and have a coarse resolution (Urraca et al., 2017; Zhang et al., 2015). In recent years, several new DSR products with higher resolution have been developed for land surface applications. Clouds, Albedo and Radiation Edition 2 data (CLARA-A2) with a 25 km resolution were published in 2017 (Karlsson et al., 2017). The Global Land Surface Satellite Downward Shortwave Radiation (GLASS-DSR) product was first generated in 2013 and has a 5 km resolution (Zhang et al., 2014). The Moderate Resolution Imaging Spectroradiometer (MODIS) land surface DSR product (MCD18A1) produced by the National Aeronautics and Space Administration (NASA) provides global 1-km resolution DSR estimates over land surfaces and has been made available to the public in 2021 (Wang, 2021). The Breathing Earth System Simulator (BESS) shortwave radiation product was released in 2017 with 5 km resolution and covers a temporal period from 2000 till now (Ryu et al., 2018). The Earth Polychromatic Imaging Camera (EPIC) data onboard the Deep Space Climate Observatory (DISCOVER/EPIC) also generate the shortwave radiation dataset with 0.1-degree resolution from 2015 to 2019 (Hao et al., 2020). However, the analyses of these high-resolutions products remain limited.

Therefore, this study aimed to comprehensively validate global daily DSR satellite products, including the CERES-SYN, CLARA-A2, GLASS, BESS, and MCD18A1. The primary goal of this study was to update the DSR satellite validation and fill data gaps over high-latitude areas. In this study, 142 global ground measurement stations were employed among which 41 are located at latitudes ranging from 60° to 90°. The spatial distributions of the data availability and accuracy, monthly variations among latitudes, and long-term trend were examined. In addition, the MCD18A1 product was used as an example to demonstrate

how potential algorithm refinements can improve the accuracy of the DSR estimation.

This study is organized as follows. The satellite products and ground measurement data are described in Section 2. The data quality control, data aggregation, and validation processes are described in Section 3. The overall accuracy of the daily DSR estimates of the five products and the analysis of the spatial distribution, intraannual analysis, interannual analysis, and quantitative analysis of potential error sources are presented and discussed in Section 4. Several strategies regarding the improvement of future algorithms are discussed in Section 5. The main conclusions are summarized in Section 6.

2. Data

2.1. Satellite DSR products

Five global satellite DSR products with different spatial resolutions were evaluated in this study. All five products are based on different methods and input data. The products are compared in detail in Table 1.

2.1.1. CERES-SYN

The CERES Synoptic (SYN1deg) product provides a global dataset of radiant fluxes at the surface, TOA, and in various atmospheric layers. The Langley Fu-Liou radiative transfer code was employed to calculate the surface shortwave radiant fluxes based on satellite observations from CERES, MODIS, geostationary data, and reanalysis data from the GEOS and other sources (Rutan et al., 2015). The CERES-SYN data span from 2000 to the present and have a 1° spatial resolution. The data have been widely used and the data accuracy has been compared with various ground measurements and other satellite products (Riihelä et al., 2017; Rutan et al., 2015; Sun et al., 2018; Yu et al., 2018).

2.1.2. CLARA-A2

The CLARA-A2 data were published by the European Organization for the Exploitation of Meteorological Satellites (EUMETSAT) Satellite Application on Climate Monitoring (CM SAF) in 2017. They are based on polar-orbiting National Oceanic and Atmospheric Administration and Metop satellite measurements from the Advanced Very High Resolution Radiometer (AVHRR). They have a global coverage and a spatial resolution of 25 km. The surface downwelling shortwave radiation was retrieved by employing the mesoscale atmospheric global irradiance code, which includes an updated version of the LUT (Mueller et al., 2009) considering the effects of aerosols, water vapor, and the surface albedo (Karlsson et al., 2013). In the second edition of CLARA data, the preprocessing of the input AVHRR level-1 TOA radiance data was improved (Karlsson et al., 2017). The CLARA-A2 now covers all cloud information, surface albedo, and surface radiation from 1983 to 2015. A new version, intended to extend the temporal coverage to 2020, will be published before 2022 (Karlsson et al., 2017).

2.1.3. GLASS-DSR

The GLASS-DSR product (Liang et al., 2021) covers the period from

Table 1
Summary of the five satellite DSR products.

Product	Spatial resolution	Coverage	Main input	Method
CERES-SYN	1° (~100 km)	2000–present	CERES, MODIS, GEOS-4/5, etc.	Radiative Transfer Code
CLARA-A2	0.25° (~25 km)	1982–2015	AVHRR	LUT
GLASS-DSR	0.05° (~5 km)	2000–2019	MODIS	Direct estimation
MCD18A1	1 km	2000–present	MODIS	LUT
BESS	0.05° (~5 km)	2000–2019	MODIS, MERRA	ANN

Table 2

Description of the 6 monitoring networks.

Network	Number	Region	Temporal resolution	Temporal coverage
NIBIO	6	Norway	1 h	2008–2018
FMI	3	Finland	1 min	1998–2019
GC-Net	17	Greenland	1 h	1995–2019
FLUXNET	103	Global	30 min, daily	1991–2014
LTER	7	Antarctic	15 min, daily	1993–2018
SURFRAD	6	United States	1 min	1995–2020

2000 to present with a spatial resolution of 5 km daily. The data are generated from the MODIS TOA spectral reflectance and surface albedo using a direct estimation approach (Zhang et al., 2019). The retrieval algorithm is composed of two major steps. First, the surface shortwave net radiation (SSNR) is calculated from the MODIS TOA reflectance based on a linear regression (Wang et al., 2015). Subsequently, the GLASS broadband albedo product is used to estimate the DSR (Zhang et al., 2019). The accuracy of the product has been validated by using Baseline Surface Radiation Network (BSRN), the Global Energy Balance Archive, and the Climate Data Center of the China Meteorological Administration (Zhang et al., 2019).

2.1.4. MCD18A1

The MCD18A1 is a recently developed global high-resolution product of the DSR based on the combination of MODIS Terra and Aqua. The product employs the LUT approach in which the TOA reflectance is used as the main input (Wang et al., 2020). Without further input, such as aerosol or cloud optical parameters, the native resolution of MODIS can be estimated (Wang et al., 2020). Version 6, which provides data from 2000 to the present at a 5 km spatial resolution and 3 h temporal resolution, is available online (Wang, 2017). Version 6.1 with a 1 km resolution was used in this study (Wang, 2021). This version is being updated; therefore, only limited data are available. Thus, the MCD18A1 was excluded from the long-term analysis in Section 4.

2.1.5. BESS shortwave radiation

BESS is a simplified process-based model which combines RTM with an artificial neural network (ANN) to generate daily DSR at 0.05° from 2000 to the present (Ryu et al., 2018). The training data are simulated from a series of MODIS atmosphere and land products as well as MERRA reanalysis data using RTM Forest Light Environmental Simulator. ANN is trained and replace the RTM to generate shortwave transmittance and then calculate DSR. The generated data has been tested over BSRN and FLUXNET stations (Ryu et al., 2018).

2.2. Ground measurements

Data were collected from 142 stations and 6 networks, with full global coverage, as shown in Fig. 1. The ancillary information of the networks is summarized in Table 1. The Surface Radiation Budget Network (SURFRAD) data from 2000 to 2019 were downloaded for long-term analysis. For the rest of the networks, the data from 2004 were used for the daily satellite product analysis.

The FLUXNET (Pastorello et al., 2020) provides global data collected at sites of multiple regional flux networks over a variety of surface types. All the stations are operated and maintained by their science teams. The temporally aggregated data after quality control are submitted to the Regional Networks and the FLUXNET Data Portal. All data were processed based on a uniform and detailed procedure developed by the European and AmeriFlux teams including data format standardization, data quality checks, gap-filling, and flux partitioning (Pastorello et al., 2020). The daily aggregated data are directly used in this study.

The SURFRAD provides data from 1993 collected at 7 sites in the United States. It has adopted measurement standards set by the BSRN, which is sponsored by the World Climate Research Program of the World Meteorological Organization. Accuracies of 2%–5% have been achieved (Augustine et al., 2000).

The Greenland Climate Network (GC-NET) consists of 24 automatic weather stations in Greenland. It provides hourly radiation observations from 2000 till now. The possible error sources have been acknowledged and the data have been calibrated by the GC-NET team (Steffen et al., 1996). To ensure the accuracy of these high latitude measurements, further quality control procedure is conducted which will be discussed in Section 3. The study also adds seven sites in the Antarctic area from the McMurdo Dry Valleys Long-term Ecological Research (LTER) project (McMurdo Dry Valleys LTER et al., 2019a; 2019b; 2019c; 2019d; 2019e; 2019f; 2019g). Both 15 min (level 1) and daily summaries (level 2) data are available, and those data have been post-processed by the LTER. Daily data from LTER are directly used in this study.

To incorporate more stations over high latitude areas, the data from the Finnish Meteorological Institute (FMI) (FMI, 2016), and the Norwegian Institute of Bioeconomy Research for emergency services and agricultural research (NIBIO) (NIBIO-LMT, 2016) are also included. As no additional documents have been found for these five datasets about their data quality, critical quality control procedures have been applied to these data which will also be discussed in Section 3.

2.3. Additional data

To examine the influence of snow cover, the Interactive Multisensor Snow and Ice Mapping System (IMS) Daily Northern Hemisphere Snow

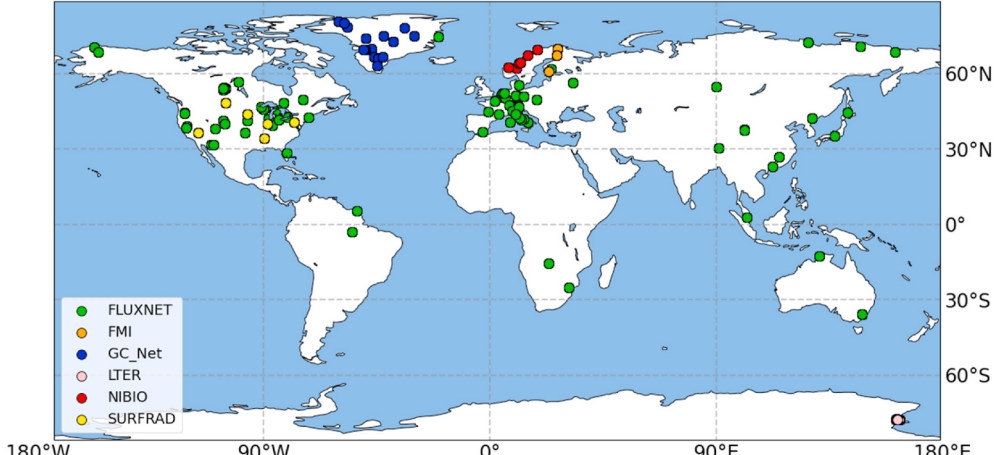


Fig. 1. Locations of the 142 ground measurement stations.

and Ice Analysis at 4 km resolution data (U.S. National Ice Center, 2008) are employed in this study. The land surface is classified into five different surface types, which are the sea, land without snow, sea ice, and snow-covered land. The data is generated by the U.S. National Ice Center and covers the Northern Hemisphere on a daily basis from 2004 (U.S. National Ice Center, 2008).

3. Methods

3.1. Quality control of the field measurements

Quality control procedures were necessary for ground measurements especially over high-latitude areas because severe conditions are common in these areas, leading to systematic or operational errors. Stations located over high-latitude areas generally have low solar zenith angles. The area affected by the shadow increases with the solar zenith angle and thus the measurement error increases (Muneer et al., 2007). In addition, snow cover and melt and freezing caused by the low temperature will lead to spurious readings during the DSR measurements.

The quality control is firstly conducted on hourly or sub-hour measurements, which are from SURFRAD, GC-Net, NIBIO, and FMI networks. The procedures include the setting of irradiance values which initially have a negative solar elevation angle of 0. Subsequently, all data pass the two limit tests of BSRN quality check (Roesch et al., 2011), which are described below:

$$\text{Physically possible limits : } -4W/m^2 < R_s < S_0 \times 1.5 \times \mu^{1.2} + 100 W/m^2 \quad (1)$$

$$\text{Extremely rare limits : } -2W/m^2 < R_s < S_0 \times 1.2 \times \mu^{1.2} + 50W/m^2 \quad (2)$$

where R_s is the DSR, S_0 is the solar constant adjusted for the Earth–Sun distance, and μ is the cosine of the solar zenith angle. Because of the unavailability of other parameters, the final procedure of the BSRN test, that is, the “across quantities” procedure, is not implemented (Roesch et al., 2011). After temporal data aggregation, the samples are also compared with satellite measurements. The stations which have more than 50 samples with standardized residuals above three for all satellite products are eliminated.

3.2. Data aggregation

Temporal data aggregation is a necessary preprocessing step, which is used to handle inconsistent temporal resolutions between *in situ* data and satellite products. The hourly data is firstly aggregated to daily. In previous research, a simple method was generally used, such as averaging hourly data, if a specific number of slots were available (Urraca et al., 2017). However, such a procedure will lead to underestimating daily values in cases with missing daytime hourly measurements (Urraca et al., 2017) and may cause large data loss, which is a critical problem over high-latitude area. Gap-filling is a possible solution, but arbitrary filling may also cause bias. A new method was developed in this study considering the tradeoff between data availability and data accuracy. The hourly data in one day were divided into eight slots by averaging three-hourly data, but only slots with more than or equal to 2 h of data were used. Subsequently, the daily average including all eight available slots was calculated. A day with random data loss can be included without compromising the data accuracy by applying this method.

For the long-term trend analysis in Section 4, all daily data were aggregated into months by calculating the mean following the methodology reported in Zhang et al. (2015). The monthly value was calculated if daily data were missing for less than nine days. The equation is as follows:

$$R_m = \frac{(\sum_{i=1}^n R_d^i)}{n} \times N \quad (3)$$

where R_m and R_d are the monthly and daily average DSR, respectively; n is the number of R_d available in one month; and N is the total number of days in the month.

3.3. Assessment metrics

The daily and monthly satellite data were validated against the ground measurement data. Several statistical indicators are available for the evaluation of the performance of solar radiation products:

Mean Bias Difference (MBD), relative Mean Bias Difference (rMBD)

$$MBD = \frac{1}{N} \sum_{i=1}^N (R_s^i - R_g^i) \quad (4)$$

$$rMBD = MBD / \bar{R}_g \quad (5)$$

Root-Mean-Square Error (RMSE), Relative Root-Mean-Square Error (rRMSE)

$$RMSE = \sqrt{\frac{1}{N} \sum_{i=1}^N (R_s^i - R_g^i)^2} \quad (6)$$

$$rRMSE = RMSE / \bar{R}_g \quad (7)$$

Mean Absolute Deviation (MAD)

$$MAD = \frac{1}{N} \sum_{i=1}^N |R_s^i - R_g^i| \quad (8)$$

where R_s represents the values predicted from satellites, R_g represents the ground measurement values, and N is the total number of observations. The rMBD and rRMSE are the main statistics; they facilitate better comparisons among different regions and seasons among these five products.

4. Results

4.1. Data availability

Different products present different levels of data loss, which strongly depends on latitude and seasonality. Fig. 2 depicts the spatial distribution of the data availability, which is defined as the number of available data divided by the total number of ground measurement data at each station. The CERES and BESS present a continuous and full coverage. The MCD18 fully covers the continents as well. The only data loss is due to the spatial mismatch between land and ocean. The availabilities of CLARA and GLASS generally reach 100% at mid- and low latitudes, but data loss occurs over high-latitude areas. To examine the reasons for this data loss, the data availability at different latitudes among different months for the five products is plotted in Fig. 3. The GLASS data availability strongly correlates with both the latitude and seasonality. The higher the latitude is, the longer the data loss exists in winter in the Northern Hemisphere. The DSR values during the polar night are colored orange. It shows that the data loss periods are longer than the polar night period, leading to a low data availability or the lack of data in winter between 50 and 70° in the Northern Hemisphere. Numerous CLARA data are lost at higher latitudes as well, but the data availability does not strongly correlate with the latitude. Furthermore, CLARA estimations over snow-covered areas have been excluded due to the reduced data accuracy (Karlsson et al., 2017).

Considering the various data availabilities of the five products, especially over high-latitude areas, only the estimated DSR, which is available for all five products, was used in the remainder of this study.

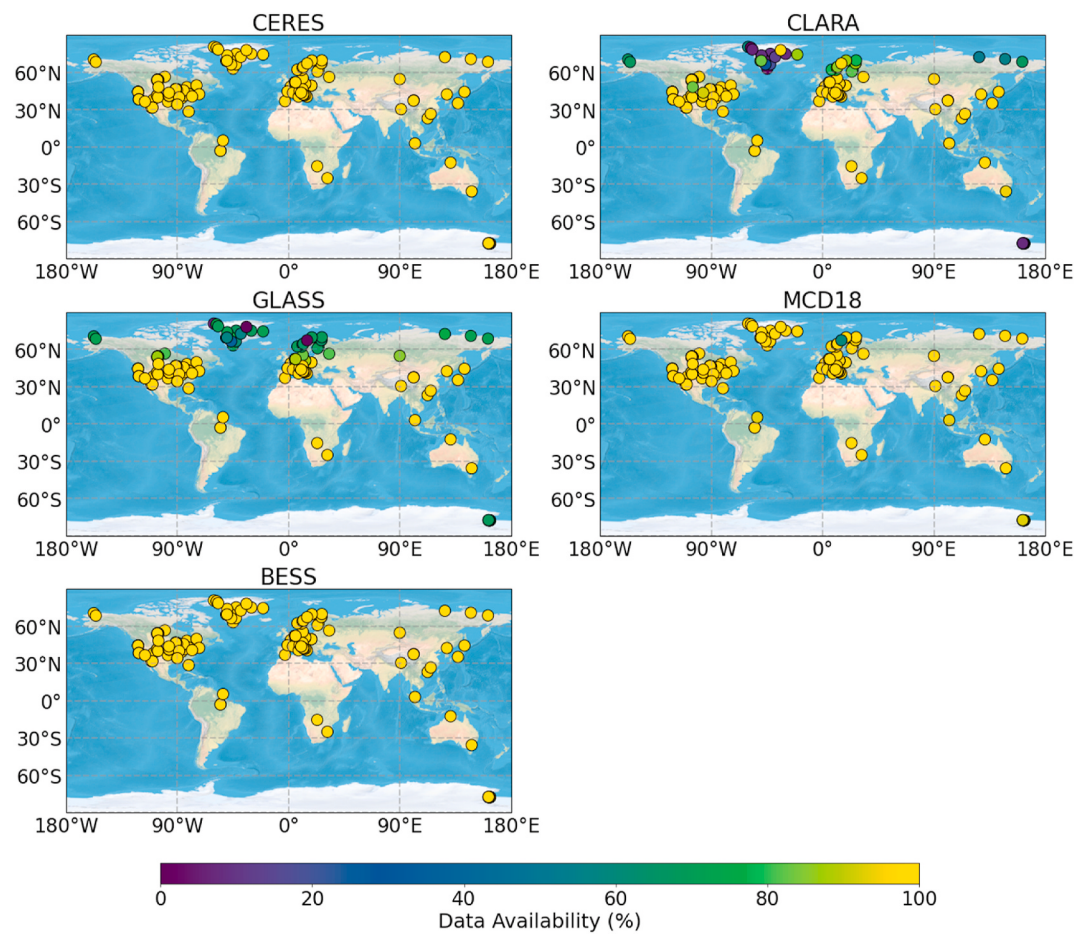


Fig. 2. Spatial distribution of the data availability on a daily time scale for all five products.

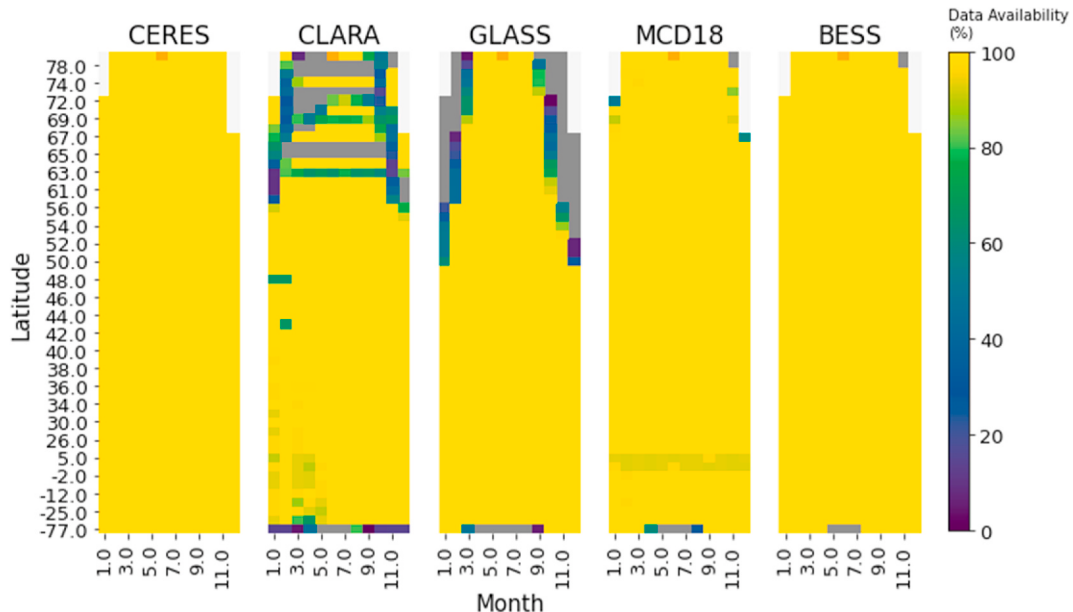


Fig. 3. Monthly distribution of the availability of five products. Gray colors represent areas for which no satellite data are available. Orange colors represent areas for which no *in situ* data are available. The white colors represent the polar night period. (For interpretation of the references to color in this figure legend, the reader is referred to the Web version of this article.)

4.2. Overall accuracies

The validations were conducted at the finest resolutions of each product, that is, at a resolution of 1, 5, 25, and 100 km, and the products with higher resolutions were aggregated for the intercomparison. The results are shown in Table 3. Overall, the RMSE of all products decreases when they are aggregated to a coarser resolution, which agrees well with the results of a previous study (Chen et al., 2019). The MCD18 is the only product that has a spatial resolution ranging from 1 to 100 km. The difference between the products with a 1 and 100 km resolution is ~5% in terms of the rRMSE. The RMSE decreases more rapidly when the products are aggregated from 1 to 5 km, but the rate of the decrease subsequently declines. The spatial aggregation process exerts considerable influence on BESS data accuracy. At its original resolution, 5 km, the rRMSE of BESS is higher than both MCD18 and GLASS, but it is lower than MCD18 and GLASS after aggregating to 100 km. Note that the accuracies of CLARA, GLASS, and MCD18 are higher at 25 km than at 100 km over high-latitude areas.

A more consistent comparison of the five products was conducted based on a spatial resolution of 1°. The detailed statistics are presented in Table 4. The performance of the five products after aggregation is similar. The overall RMSE falls in the normal range of the daily validation, that is < 35 W/m² (Huang et al., 2019; Wang et al., 2020). However, the rRMSE is slightly higher than that reported in previous studies (Urraca et al., 2017; Wang et al., 2020), primarily because more stations were located over high-latitude areas. The CERES presents the lowest RMSE of 27.6 W/m² and highest R² of 0.916. The high-resolution products have a slightly higher RMSE, which is 29.1, 30.3, 29.6, and 31.6 W/m² for CLARA, GLASS, BESS, and MCD18, respectively. One possible reason for this difference might be that these four DSR products with high spatial resolution are mainly derived from polar-orbiting satellite data with limited daily observations, which is a major error source in dynamically atmospheric conditions. In addition, three-dimensional cloud radiative effects will lead to more uncertainties in high-resolution products combined with the limited daily observations (Chen et al., 2019). The CERES tends to overestimate the DSR, whereas the other four products underestimate the DSR. The CLARA is the least biased among all five products.

The reliability of the results also strongly depends on the accuracies of the ground measurements. In Fig. 4, the retrievals of different products are plotted against the measurements of different networks. FLUXNET stations have a full global coverage and provides most measurements, and consequently validation results over FLUXNET stations dominate the overall results in Table 4. The SURFRAD only has limited stations in the United States but the accuracy of this network is the highest because it provides 1 min measurements and has processed the highest level of calibrations set by the BSRN. Based on the comparison of these two networks, CERES achieves the most consistent results with an rRMSE of 16.8%. The GLASS performs the worst over SURFRAD stations, whereas the MCD18 presents the lowest accuracy over FLUXNET stations. The NIBIO and FMI are two networks located at high latitudes, which are monitored by European countries. The accuracies of these two networks have been verified (Urraca et al., 2017). With respect to these two networks, CLARA achieves the highest accuracies with an rRMSE of 17.8% and 18.4%, respectively. BESS has the highest rRMSE, 22.3%, and 22.4%, respectively, over these two networks. The GC-Net and LTER stations are in Arctic and the Antarctic regions, respectively. The rRMSE over these two networks significantly increases for all five products and MCD18 is significantly biased compared with the other four products. This is partly due to the limitations of existing algorithms over high-latitude areas. However, the accuracies of the ground measurements must also be considered. The performances of these five products slightly vary over different networks, but the overall results are comparable.

Table 3
Accuracies of each product at different spatial resolutions.

Latitude	Product	100 km		25 km		5 km		1 km					
		R ²	rMBD (W/m ²)	RMSE (W/m ²)	rRMSE (%)	R ²	rMBD (W/m ²)	RMSE (W/m ²)	rRMSE (%)	R ²	rMBD (W/m ²)	RMSE (W/m ²)	rRMSE (%)
0–30	CERES	0.86	11.8	6.6	30.1	16.8	20.2	0.83	23.7	13.3	41.0	23.0	20.9
	CLARA	0.85	21.5	12.0	36.1	33.6	18.8	0.81	13.6	7.6	35.5	19.9	21.7
	GLASS	0.81	10.2	5.7	38.9	21.8	0.8	3.0	1.7	33.7	18.9	0.76	3.9
	BESS	0.73	-1.1	-0.6	30.8	17.2	0.83	3.7	2.1	31.6	17.7	0.81	2.5
	MCD18	0.82	0.0	0.0	25.3	15.8	0.91	-7.7	-4.7	31.6	19.6	0.90	-7.8
30–60	CERES	0.93	0.2	0.1	34.3	23.8	26.1	16.2	0.93	-4.0	-2.5	27.5	17.1
	CLARA	0.93	-3.6	-2.2	36.2	25.1	0.85	-3.2	-2.2	35.6	21.2	0.88	2.5
	GLASS	0.91	-4.8	-3.0	31.5	21.8	0.88	3.7	2.6	30.3	25.5	0.81	-9.7
	BESS	0.92	-3.9	-2.5	33.7	23.4	0.84	-9.9	-6.9	30.7	19.0	0.89	-3.6
	MCD18	0.92	-8.5	-5.3	29.6	18.4	0.91	-7.7	-4.7	31.6	19.6	0.90	-4.8
60–90	CERES	0.86	6.7	4.6	34.3	23.8	28.7	17.9	0.9	-1.6	-1.0	30.4	24.8
	CLARA	0.85	-5.4	-3.7	36.2	25.1	0.85	-3.2	-2.2	35.6	21.2	0.88	3.6
	GLASS	0.88	2.6	1.8	31.5	21.8	0.88	3.7	2.6	30.3	25.5	0.81	-6.8
	BESS	0.87	-11.0	-7.6	33.7	23.4	0.84	-9.9	-6.9	30.7	19.0	0.85	-10.1
	MCD18	0.84	-14.2	-9.8	38.7	26.8	0.86	-10.2	-7.1	34.4	24.0	0.85	-7.0
All	CERES	0.92	2.2	1.3	27.6	17.0	29.1	17.9	0.9	-1.6	-1.0	30.4	18.7
	CLARA	0.91	-1.5	-0.9	30.3	18.6	0.89	-2.9	-1.8	31.9	19.5	0.88	-2.9
	GLASS	0.9	-2.8	-1.7	29.6	18.2	0.89	-3.1	-1.9	32.3	19.8	0.87	-3.1
	BESS	0.91	-3.4	-2.1	31.6	19.4	0.9	-6.8	-4.2	32.6	20.0	0.88	-7.1
	MCD18	0.9	-8.0	-4.9	22.6	17.0	28.7	17.9	0.9	-1.6	-1.0	30.4	18.7

Table 4

Summary of the statistics of each product for different subareas.

Latitude ($^{\circ}$)	Product	R^2	MBD (W/m^2)	rMBD (%)	RMSE (W/m^2)	rRMSE (%)	MAD (W/m^2)	rMAD (%)
All	CERES	0.916	2.2	1.3	27.6	17.0	19.6	12.0
	CLARA	0.911	-1.5	-0.9	29.1	17.9	20.3	12.5
	GLASS	0.899	-2.8	-1.7	30.3	18.6	21.7	13.3
	MCD18	0.904	-8.0	-4.9	31.6	19.4	22.6	13.9
	BESS	0.907	-3.4	-2.1	29.6	18.2	21.3	13.1
60–90	CERES	0.860	6.7	4.6	34.3	23.8	24.1	16.7
	CLARA	0.846	-5.4	-3.7	36.2	25.1	23.5	16.2
	GLASS	0.878	2.6	1.8	31.5	21.8	22.0	15.3
	MCD18	0.840	-14.2	-9.8	38.7	26.8	26.1	18.1
	BESS	0.875	-11.0	-7.6	33.7	23.3	24.1	16.7
30–60	CERES	0.932	0.2	0.1	25.3	15.8	18.3	11.4
	CLARA	0.931	-3.6	-2.2	26.1	16.2	18.6	11.6
	GLASS	0.915	-4.8	-3.0	28.7	17.8	20.7	12.9
	MCD18	0.922	-8.5	-5.3	29.6	18.4	21.4	13.3
	BESS	0.924	-3.9	-2.4	27.3	17.0	20.1	12.5
0–30	CERES	0.856	11.8	6.6	30.1	16.8	22.8	12.7
	CLARA	0.852	21.5	12.0	36.1	20.2	28.9	16.1
	GLASS	0.807	10.2	5.7	33.6	18.8	26.1	14.6
	MCD18	0.824	0.0	0.0	30.8	17.2	23.8	13.3
	BESS	0.726	-1.14	-0.6	38.9	21.6	24.7	13.8

4.3. Spatial distribution

Fig. 5 depicts the spatial distributions of the rMBD and rRMSE of the five products. The figure shows that all five products present latitudinal variations, with the lowest deviations and RMSEs in mid-latitude regions. The statistics for different latitude zones are listed in Table 2. Over low-latitude areas, CERES and MCD18 have the highest accuracies with a RMSE of $30.1\text{ W}/m^2$ (16.8%) and $30.8\text{ W}/m^2$ (17.2%), respectively. Almost no bias was observed for the MCD18 product. In contrast, BESS yields the worst accuracy over low-latitude areas, with the largest RMSE of $38.9\text{ W}/m^2$ (20.2%) and MBD of -1.14 (-0.6\%) , followed by CLARA with the largest MBD of $21.5\text{ W}/m^2$ (12%) and RMSE of $36.1\text{ W}/m^2$ (18.8%). Both the GLASS and CERES tend to overestimate the DSR over low-latitude areas and have a bias of $11.8\text{ W}/m^2$ (6.6%) and $10.2\text{ W}/m^2$ (5.7%), respectively. The accuracies of the CERES data are outstanding, with the lowest RMSE for each subregion, especially over mid-latitude areas. As shown in Table 2, the MBD over mid-latitude areas is close to $0.2\text{ W}/m^2$ (0.1%) and the RMSE is the lowest among all products. In addition, CLARA and BESS also yield low RMSE over mid-latitude areas, which are, $26.1\text{ W}/m^2$ (16.2%) and $27.3\text{ W}/m^2$ (17%) respectively. Over high-latitude areas, all product degrade with significant increase of rRMSE. GLASS shows the best performance, with a bias of $2.6\text{ W}/m^2$ (1.8%) and the lowest RMSE of $31.5\text{ W}/m^2$ (21.8%). The MCD18 significantly underestimates the DSR, with an MBD of $-14.2\text{ W}/m^2$ (-9.8%). However, because only available data for all products are kept over high-latitude areas, several degraded results of one product may be excluded from the data loss of other products. In summary, the latitude influences the products significantly, especially for CLARA, BESS, and MCD18. The magnitude of underestimation of BESS and MCD18 amplified from tropical areas to high latitude areas, while CLARA overestimates in low latitude area but tend to underestimate as latitude increases.

The products also have several other similar spatial distribution characteristics. First, significant deviations are mostly observed near the coastal region. Most of the overestimations of CERES and CLARA were observed along the coastline. These results agree well with previous studies' findings (Urraca et al., 2017; Zhang et al., 2015). Ocean fraction data from the CERES-SYN product were employed to further examine the effect of ocean presence in the pixel. An ocean fraction above and below 70% was defined as coastal and inland pixel, respectively. Fig. 6 depicts the rRMSEs and rMBDs of the five satellite products for inland and coastal areas. Significant overestimation can be observed for CLARA and CERES over coastal regions compared with inland regions. The

GLASS, BESS, and MCD18 tend to underestimate the DSR in the coastal region, but the magnitude of the underestimation insignificantly differs depending on the location. BESS is most influenced by the ocean, with rMBD increase from -2.0% to -4.5% and rRMSE increase from 18.3% to 21.3% . Although the rRMSEs of the other four products are less influenced by the presence of the ocean, a difference can be noted over the inland area, where CERES and CLARA perform better than GLASS and MCD18. Opposite results were obtained over the coastal area. The rRMSEs of CERES, CLARA, GLASS, and MCD18 over coastal zone are 17.6% , 16.7% , 15.8% , and 15.7% , respectively, demonstrating that the estimation accuracy of the DSR in these regions is higher at higher product resolution. These results may indicate that the identification of land or ocean along the coast improves based on high-resolution satellite products, leading to decreased uncertainties related to the change in the terrain type.

4.4. Intraannual analysis

Fig. 7 shows the heatmap of the intraannual variation of the monthly rMBD and rRMSE for different latitude intervals in the Northern Hemisphere. Grids without data were plotted in gray for all five products. The rMBDs of all products over areas with latitudes ranging from 0 to 30° do not indicate notable intraannual trends. For the area between 30° and 55° , the products tend to underestimate the DSR during the winter, but the results are comparatively accurate from April to September, which agrees with previous results obtained for CLARA (Urraca et al., 2017). This trend is especially pronounced for MCD18. The CERES is less dependent on the seasonal change at mid-latitudes. When the latitude reaches 55° – 80° , a seasonal shift in the rMBD can be observed for all five products. The CERES, CLARA, and GLASS slightly overestimate the DSR from June to August, whereas the BESS yields comparatively accurate results. In winter, CLARA, GLASS, BESS, and MCD18 tend to underestimate the DSR over high-latitude areas and the MCD18 is the most biased among the products.

With respect to the rRMSE, all products present a similar pattern. The rRMSE is low from June to August and subsequently increases in fall and winter. The higher the latitude is, the longer the high rRMSE lasts. The lowest rRMSEs were observed over mid-latitude areas, which agrees with our previous conclusions. The rRMSE slightly increases in low-latitude areas, but a seasonal trend, similar to that in the high-latitude region, is not notable.

Based on the combination of the results from all plots, we can

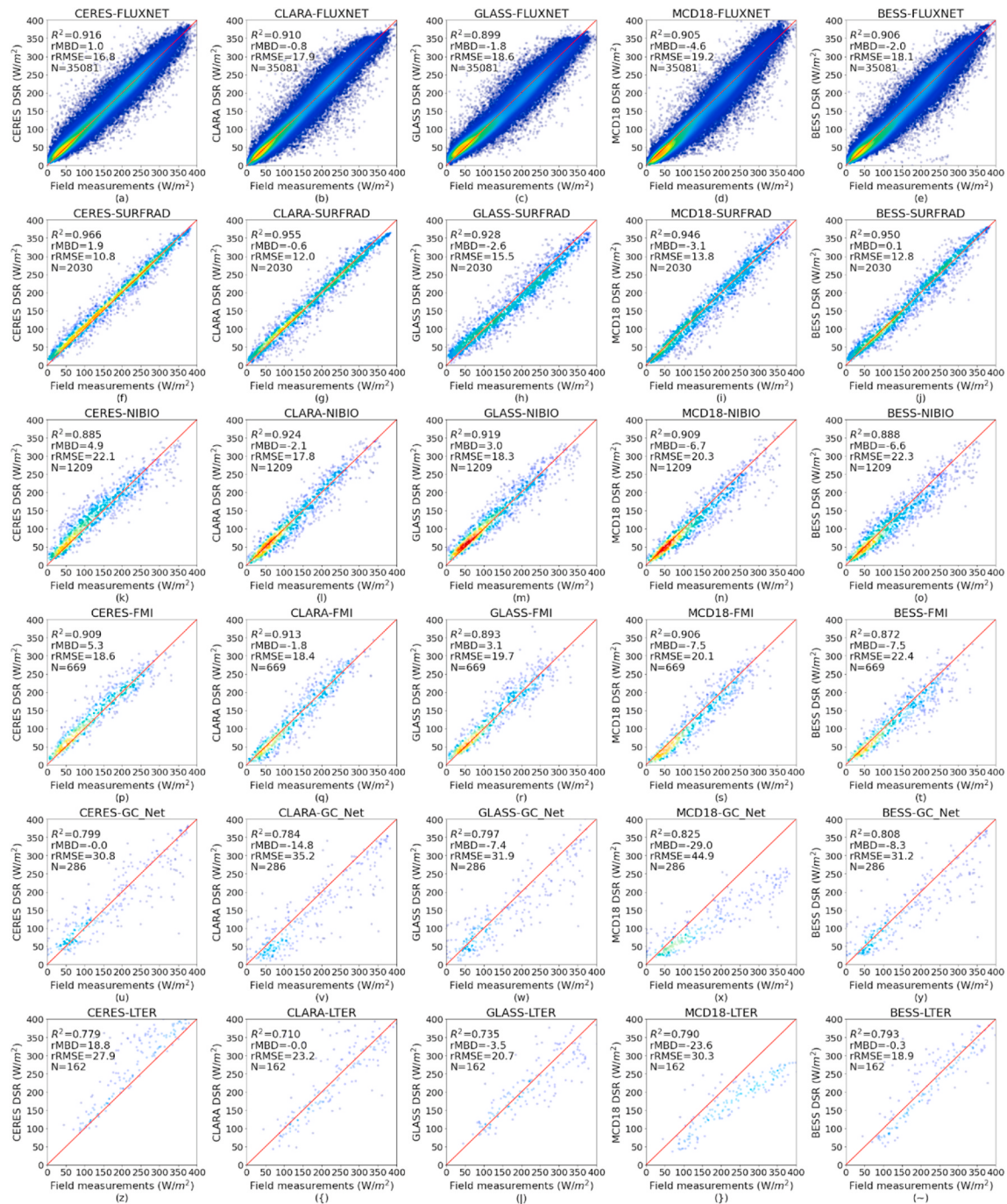


Fig. 4. Scatter plots of the five products over different networks.

conclude that the season affects the DSR estimation. The accuracies of all five products decrease in winter and the seasonal effect slightly varies with the latitude. The higher the latitude is, the more notable is the annual trend in terms of the rMCD and rRMSE. All five products yield comparable results during the summer over mid-latitude areas. However, the absolute rMBD increases in winter, which leads to a high rRMSE. The seasonal dependence of each product varies. The MCD18 has the earliest responds to seasonal changes, followed by GLASS, CLARA, and BESS. The seasonal and spatial variations may indicate that snow is one of the major factors contributing to large biases and inaccuracies in satellite DSR estimations, especially for MCD18, because the similar optical and reflection characteristics between snow and clouds lead to difficulties in the identification of snow-covered periods and thus

to underestimations over snow-covered surfaces (Huang et al., 2019).

To better support this argument, more analyses of snow were conducted. The IMS Daily Northern Hemisphere Snow and Ice Analysis at 4 km resolution data (U.S. National Ice Center, 2008) were employed. Fig. 8 presents the rMBD and rRMSE over snow-covered and snow-free areas. Because snowy regions are generally located over high-latitude areas in which other sources may also lead to uncertainties, we only selected SURFRAD stations for the comparison. The results show that snow indeed leads to uncertainties in the DSR estimation. All five products yield higher RMSEs over snow-covered surfaces, but the magnitudes vary depending on the product. The MCD18 is most influenced by the snow, with a rRMSE of 13.1% over land and a rRMSE of 40.3% over snow-covered regions. The MCD18 significantly

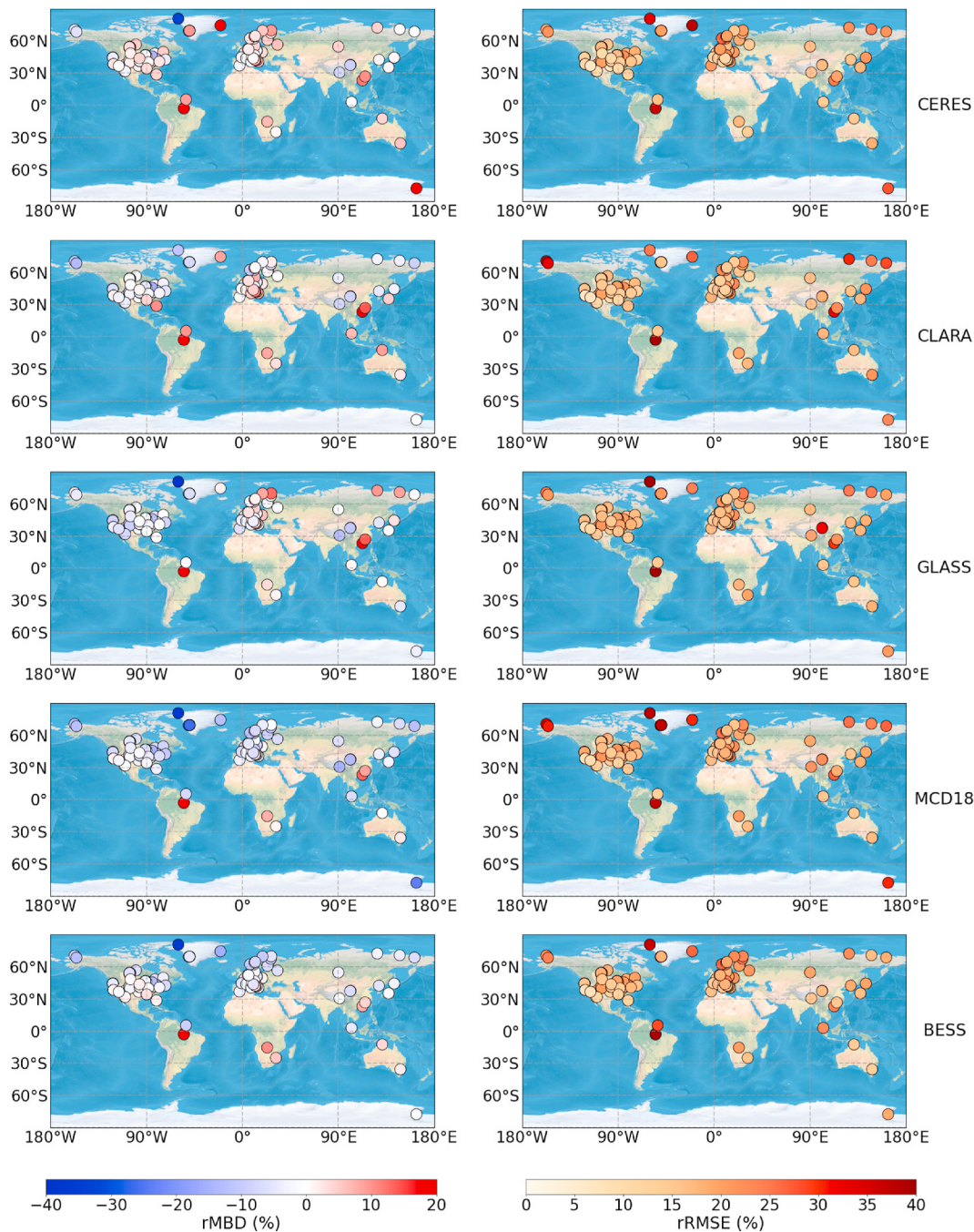


Fig. 5. Spatial distributions of the rMBDs and rRMSEs of the satellite-estimated DSR and ground measurements for CERES, CLARA, GLASS, MCD18, and BESS on a daily time scale.

underestimates the DSR over snow-covered areas. The GLASS is also substantially affected by snow, with rRMSE increases from 14.9% over land to 38.6% over snow-covered regions, and overestimations were observed over snow-covered regions. Although CLARA already excludes strongly degraded estimates over snow-covered surfaces, the current rRMSE still reaches 36.0%. BESS is less influenced by the snow in terms of rRMSE, but BESS indeed significantly underestimate DSR when snow present with rMBD changing from positive 0.4% to negative 8.1%. The CERES performs the best over snow-covered regions, with a rRMSE of 24.3%.

4.5. Interannual analysis

The results of previous studies indicated a pronounced brightening trend during the 1990s, but the trend diminishes or even reverses starting in 2000 (Hatzianastassiou et al., 2005; Hinkelmann et al., 2009; Wild et al., 2009; Zhang et al., 2015). However, the latest global trend analysis based on satellite products was conducted using data obtained before 2012 (Zhang et al., 2015). The ~20-year long data records of four satellite products and associated long-term measurements archived by three SURFRAD stations allow us to revisit this matter. Because limited MCD18 data have been released, only the long-term trend of CERES, GLASS, CLARA, and BESS were analyzed in this study. Fig. 9 depicts the annual average DSR estimate and values measured from 2001 to 2018.

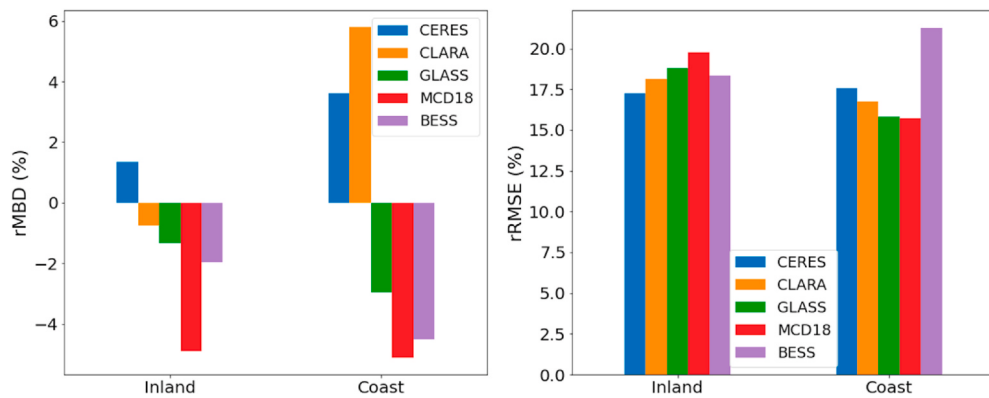


Fig. 6. Comparison of the rMBD and rRMSE over inland and coastal areas.

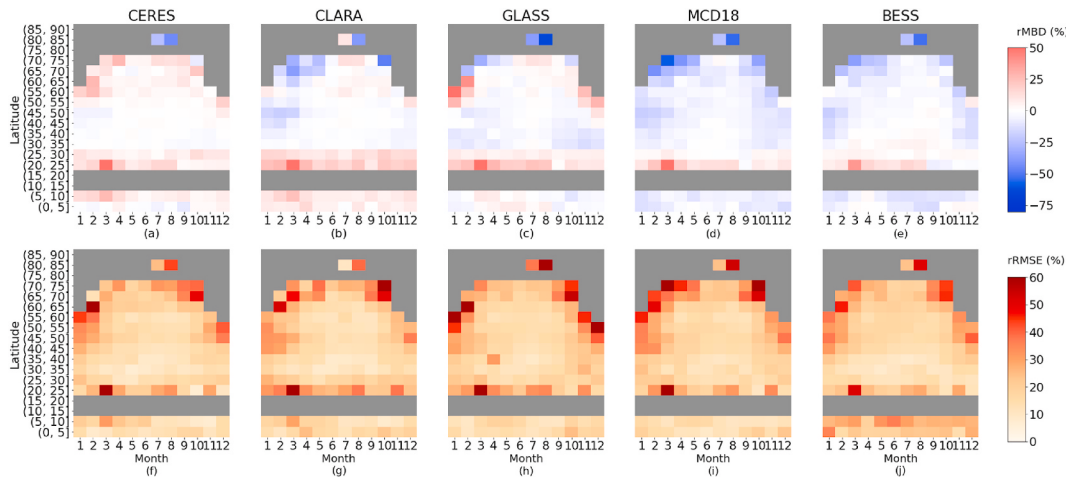


Fig. 7. The rMBDs and rRMSEs of daily values over the Northern Hemisphere were calculated for each month and each latitude interval. The rMBD is shown in (a), (b), (c), (d), and (e). The rRMSE is shown in (f), (g), (h), (i), and (j). The gray color represents areas for which no data were available. Polar night data were excluded. (For interpretation of the references to color in this figure legend, the reader is referred to the Web version of this article.)

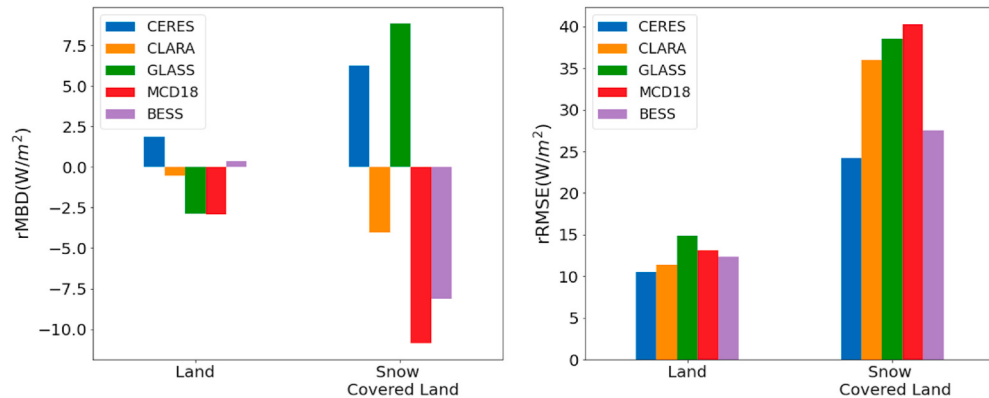


Fig. 8. Comparison of the rMBD and rRMSE values obtained over snow-covered and snow-free areas.

All four satellite products are consistent with the ground measurements. The CERES, BESS, and CLARA can explain most of the interannual variabilities, with correlation coefficients of 0.95, 0.91, and 0.90, respectively, further demonstrating that satellites can be used to monitor interannual variability. In our study, *in situ* data show insignificant brightening or dimming trends over the past two decades, with an annual slope of 0.004 W/m². The CERES and BESS data agree well with the *in situ* results, with an annual slope of 0.049 W/m² and 0.034 W/m². CLARA demonstrates a slight dimming trend (-0.193 W/m² per year)

and GLASS data present a significant dimming trend (-0.383 W/m² per year). Fig. 9 also proves that CERES tends to overestimate the DSR, whereas CLARA, BESS, and GLASS have underestimated the DSR during the past two decades.

To examine the stabilities of the current satellite DSR products and determine if they can detect long-term trends, which is especially useful for climate change analysis, the bias and RMSE were monitored over the long term in this study using SURFRAD data. The interannual evolution of the annual aggregated bias and the RMSE from 2001 to 2009 are

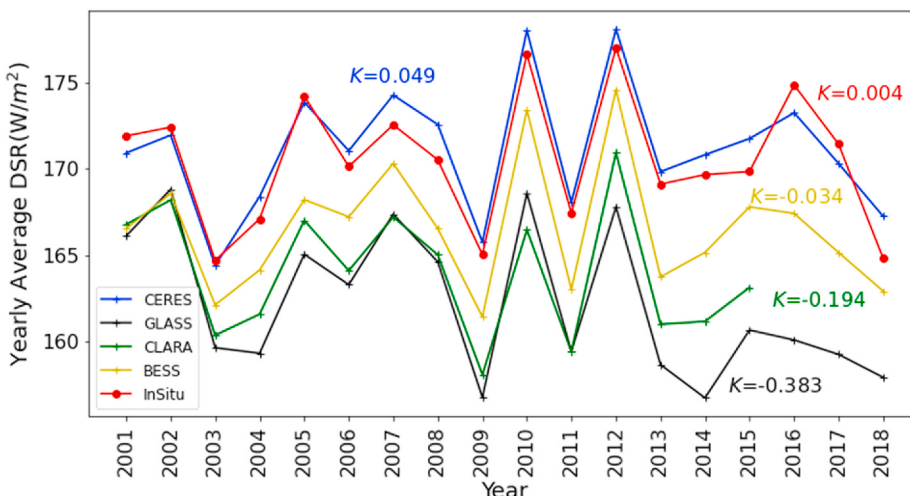


Fig. 9. Annual average DSR from 2001 to 2019. The slope (K) is labeled for each product.

plotted for four products in Fig. 10. BESS and CERES show stable consistencies with the ground measurement values because both the bias and RMSE have not changed during the past two decades. However, CLARA and GLASS data exhibit abnormal changes. Both the deviation and RMSE of these two products increase over the years. The slope of the increase in the annual bias reaches -0.250 and -0.387 W/m^2 for CLARA and GLASS, respectively, which contributes to a change of $\sim 7.8 \text{ W/m}^2$ for GLASS after two decades and a change of 3.75 W/m^2 for CLARA after 15 years. The annual RMSEs of CLARA and GLASS also significantly change, with slopes of 0.357 and 0.310 W/m^2 , respectively. The changes may be related to sensor degradation. Previous publications have pointed out that Terra MODIS presents a significant degradation, especially at shorter wavelengths (D. Wang et al., 2012). The stability of BESS and CERES also indicates that using higher level of MODIS products and the incorporation of various inputs from different data sources may help avoid the influence of sensor degradation. The long-term drifting trend disagrees with the results reported by Urraca et al. (2017) who reported the temporal stability for CLARA data from 2005 to 2015, which might be due to several reasons. First, our study includes a much longer time scale, which may lead to a more notable trend. Furthermore, Urraca et al.'s (2017) research focused on the European area, with latitudes ranging from 35° to 65° , whereas our study includes data for the United States, with latitudes ranging from 30° to 50° . As mentioned before, the latitude affects the accuracy of the satellite products, which may lead to different long-term trends. This also explains why both CLARA and GLASS have exhibited a dimming trend over the past two decades in contrast to the ground measurement results shown in Fig. 9.

4.6. Cloud analysis

Cloud coverage and cloud visible optical depth also directly affect the estimation of DSR. In this study, cloud coverage and cloud visible optical depth data from the CERES-SYN dataset were used to examine the cloud effect. As shown in Fig. 11, the rRMSE linearly increases with increasing cloud coverage for all five satellite products. The coefficients of the correlations between the rRMSE and cloud coverage are 0.94 , 0.95 , 0.94 , 0.97 , and 0.93 for CERES, CLARA, GLASS, MCD18, and BESS respectively. Similar strong correlations were observed between the rRMSE and cloud optical depth. In addition, an extreme high cloud fraction and cloud optical depth also lead to significant biases in all five products. The MCD18 tends to underestimate the DSR in areas that are fully covered by clouds or in which the cloud optical depth is high. The CERES, CLARA, BESS, and GLASS tend to overestimate the DSR when the cloud optical depth is high, but correlations with the cloud area

fraction were not observed. Comparing the five products, the CLARA is less biased when the cloud area fraction is high and MCD18 is less biased when the cloud visible optical depth is high.

5. Potential algorithm refinements

The DSR products with high spatial resolution, such as MCD18A1, CLARA-A2, BESS, and GLASS, can resolve the fine spatial variability of solar radiation. However, the current accuracies of these products remain slightly lower than that of the mature CERES product. In response to the issues of current high resolution DSR products, two possible refinements are suggested in this study. The MCD18 is used as an example. As indicated by the above-mentioned analysis, the compromised performance of the retrieval algorithm over snow-covered surfaces will cause the overall degradation of the accuracy. The investigation of the reasons for this performance difference showed that the TOA reflectance of the blue band is used in the original LUT algorithm implemented in the MCD18 data generation to derive atmospheric transmittance and scattering parameters. Although blue band data provide an informative contrast between surface and atmosphere contributions over dark surfaces, the blue band-based approach loses its effectiveness over bright surfaces such as snow-covered pixels. To address this issue related to the reduced sensitivity of the TOA surface of the blue band to the DSR, the shortwave infrared channel should be used for snow-covered surfaces (Fig. 12). Snow-covered pixels observed by Aqua/MODIS data over seven SURFRAD sites in 2013 were used in the comparison. The validation confirms that the DSR over snow-covered pixels is significantly underestimated based on the use of the blue band method, which aligns with the assessment results of the MCD18A1 product. Based on the comparison, the use of shortwave infrared band will substantially improve the DSR estimation. The RMSE decreases by 82.8 W/m^2 and the bias declines by 54.6 W/m^2 .

Another possible reason for the performance difference between CERES and other four high spatial resolution DSR products might be that all four DSR products with high spatial resolution evaluated in this study are mainly based on polar-orbiting satellite data. In contrast, the CERES product employs geostationary data for diurnal interpolation (Doelling et al., 2013). Although polar-orbiting sensors enable global coverage and an increased sampling frequency over high latitudes, they can only provide limited observations in low- and mid-latitude areas. The limited number of daily observations could be a major source of uncertainties in cases with dynamically changing atmospheric conditions. Previous studies have applied different methods on geostationary sensors like advanced Himawari imager (AHI) and Advanced Baseline Imager (ABI) to estimate DSR and achieved promising results (Ma et al., 2020; Yi

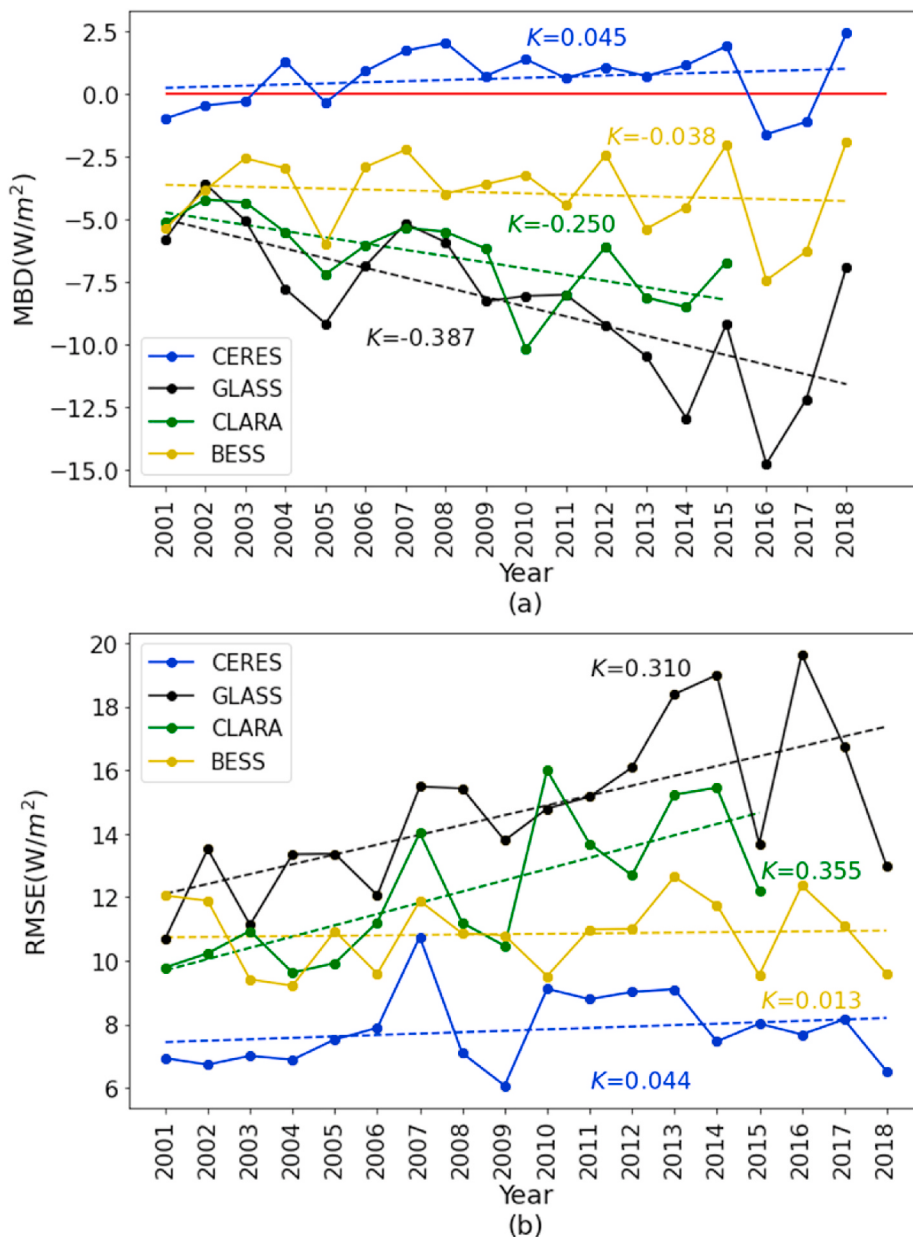


Fig. 10. (a) Annual bias (MBD) from 2001 to 2019, (b) Annual RMSE from 2001 to 2019. The slope (K) is labeled for each product.

Zhang et al., 2020). In this study, we applied the LUT algorithm to Advanced Baseline Imager (ABI) data acquired by the Geostationary Operational Environmental Satellite (GOES) – 16 and combined with MODIS data to improve the estimation accuracy.

Fig. 13 shows an example of a time series of diurnal DSR changes measured at Fort Peck, MT, using the SURFRAD network. In this example, the ABI 15-min retrievals agree very well with the field measurements. The decrease in the DSR in the local morning caused by morning clouds is accurately captured by the ABI data with high-temporal resolution. In contrast, although MODIS data yield accurate instantaneous values corresponding to the satellite overpass time, the daily value suffers from large uncertainties. The feasibility of geostationary satellite data for estimating the daily DSR can be demonstrated based on the quantitative validation with the SURFRAD measurements (Fig. 14). The RMSE of the ABI daily results is low (24.7 W/m^2), that is, 8.6 W/m^2 less than that of the MODIS results, and is comparable with previous studies on geostationary sensors (Ma et al., 2020; Yi Zhang et al., 2020). Subsequently, the optimal interpolation approach was

applied to combine the ABI and MODIS data (Wang and Liang, 2014), further reducing the RMSE to 19.3 W/m^2 .

6. Conclusions

In this study, daily DSR estimated derived from five global satellite products, namely, CERES-SYN, CLARA-A2, GLASS-DSR, MCD18A1, and BESS were evaluated. The products were compared at various resolutions ranging from 1 to 100 km. A full examination was conducted at a resolution of 1° in terms of the spatial, intraannual, and interannual analyses of the global product accuracies with focus on high-latitude areas.

CERES, BESS, and MCD18 have a full global coverage, while GLASS and CLARA present data loss over high latitude area in winter and summer over the Northern Hemisphere respectively. The accuracies of all products increased when the data were aggregated from 1 to 100 km. The rate of the increase declined with decreasing resolution. The most accurate results were retrieved at 25 km over high latitude areas for

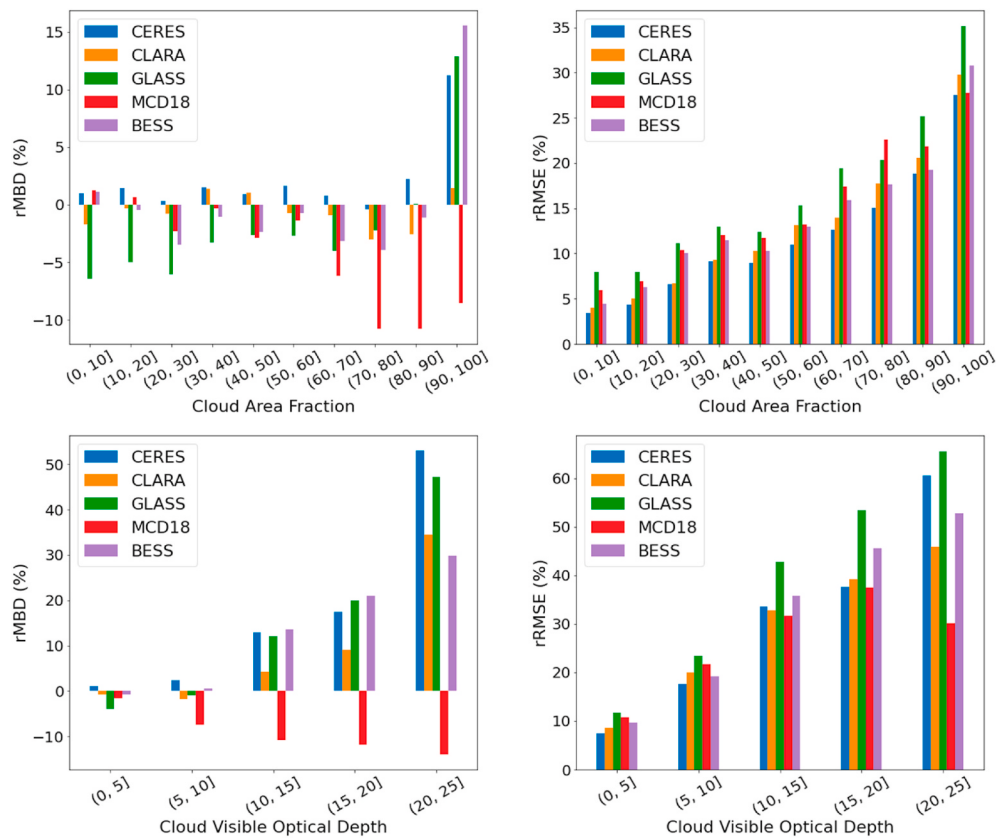


Fig. 11. Correlations between the rMBD and rRMSE and the cloud area fraction and cloud visible optical depth.

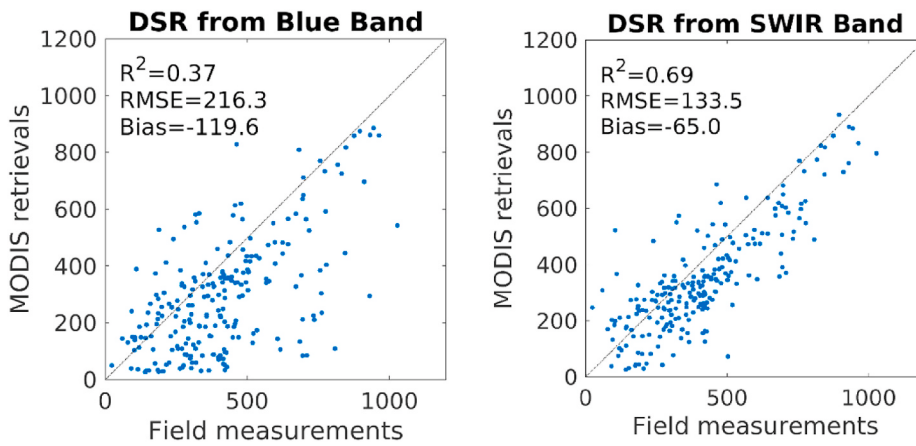


Fig. 12. Comparison of the DSR retrieval results based on different band selection strategies.

most products. After aggregation to a resolution of 1° , the RMSEs of CERES, CLARA, GLASS, BESS, and MCD18 daily data were 27.6, 29.1, 30.3, 29.6, and 31.6 W/m^2 , respectively. Although the high-resolution products present an overall higher RMSE, they have a potential capacity for accurately estimating the DSR over complex terrain such as the coastal region. All products indicate that the latitude has a significant effect on the DSR estimation. The most accurate DSR retrievals were obtained over mid-latitude areas. The latitude also affects the intra-annual change of the estimation accuracy. A seasonal trend was not observed over low-latitude areas, whereas high rRMSE and absolute rMBD are presented in winter over mid-to high-latitude areas. The high rRMSEs over high-latitude regions in winter in the Northern Hemisphere strongly correlate with the snow-covered area, which is indistinguishable from clouds. The results show that the rRMSEs of all high-resolution

products increase more than 20% in snow-covered areas than those in snow-free areas. Clouds also affect the DSR estimations based on all five products. A higher cloud visible optical depth and cloud fraction are associated with a higher rRMSE for all products.

An analysis examining the long-term trend from 2001 to 2018 was conducted based on the monthly data from four satellite products. Both *in situ*, BESS, and CERES data have exhibited a flat trend in the past two decades, whereas CLARA and GLASS data show a dimming trend. The absolute bias and RMSE of CLARA and GLASS have continuously increased over the past two decades, while both CERES and BESS remain stable. Note that this study is only based on a limited number of SURFRAD stations in mid-latitude areas. The observed changes of different satellite products may be influenced by the latitude as well. Additional ground measurement data should be used in future research

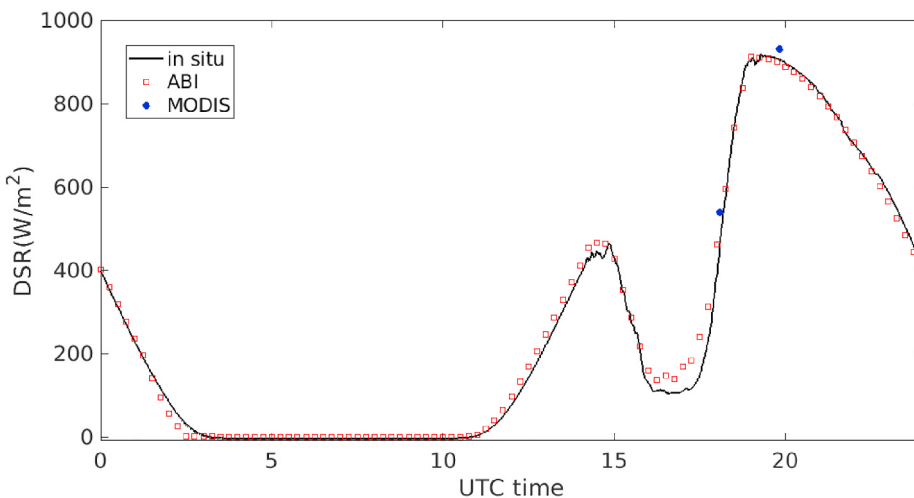


Fig. 13. Diurnal variation of the downward shortwave radiation based on *in situ* measurements and satellite estimates obtained on June 10, 2018, at Fort Peck, MT.

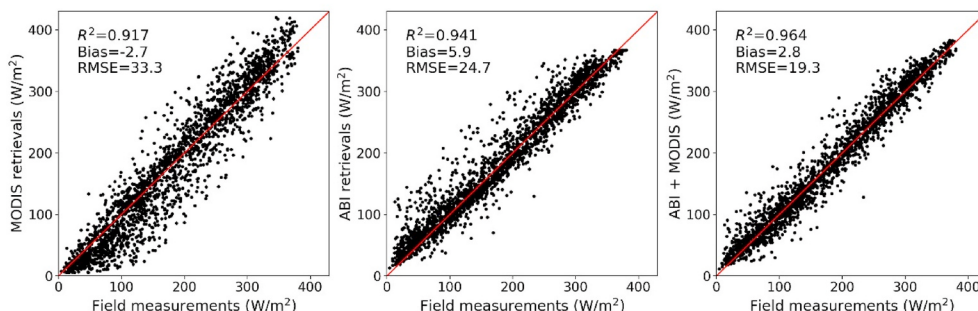


Fig. 14. Validation results of the daily downward shortwave radiation retrieved from ABI and MODIS data.

to examine global changes.

The four global DSR products with high spatial resolution evaluated in this study have slightly worse accuracies than the mature CERES product, mainly because of their degraded performance over snow-covered cases and the limited temporal sampling provided by polar-orbiting satellite data. Based on the proposed algorithm refinements, which address these two issues, the DSR retrieval accuracy can be substantially improved.

Declaration of competing interest

The authors declare that they have no known competing financial interests or personal relationships that could have appeared to influence the work reported in this paper.

Acknowledgments

This study is supported by NASA under grant 80NSSC18K0620 and 80NSSC21K0701. We would like to thank the SURFRAD, FLUXNET, McMurdo Dry Valleys LTER, and GC-Net science teams for maintaining and providing their measurement data. We also appreciate the two national networks, SMHI and NIBIO, for their high-quality measurement data. We would also like to acknowledge the NASA Langley Research Center for providing CERES-SYN data, the EUMETSAT CM SAF project for providing CLARA-A2 data, NASA MODIS Land Science Team for providing MCD18A1 satellite data, the Environmental Ecology Lab of Seoul National University for providing BESS data. The GLASS-DSR data are published by the University of Maryland (<http://www.glass.umd.edu/>).

References

- Augustine, J.A., DeLuisi, J.J., Long, C.N., 2000. SURFRAD—A national surface radiation budget network for atmospheric research. *Bull. Am. Meteorol. Soc.* 81 (10), 2341–2358.
- Boilley, A., Wald, L., 2015. Comparison between meteorological re-analyses from ERA-Interim and MERRA and measurements of daily solar irradiation at surface. *Renew. Energy* 75, 135–143. <https://doi.org/10.1016/j.renene.2014.09.042>.
- Brown, M.G.L., Skakun, S., He, T., Liang, S., 2020. Intercomparison of machine-learning methods for estimating surface shortwave and photosynthetically active radiation. *Rem. Sens.* 12 (3), 372.
- Chen, L., Yan, G., Wang, T., Ren, H., Hu, R., Chen, S., Zhou, H., 2019. Spatial scale consideration for estimating all-sky surface shortwave radiation with a modified 1-D radiative transfer model (No. 3). <https://doi.org/10.1109/JSTARS.2019.2896644>.
- Doelling, D.R., Loeb, N.G., Keyes, D.F., Nordean, M.L., Morstad, D., Nguyen, C., Wielicki, B.A., Young, D.F., Sun, M., 2013. Geostationary enhanced temporal interpolation for CERES flux products. *J. Atmos. Ocean. Technol.* 30 (6), 1072–1090. <https://doi.org/10.1175/JTECH-D-12-00136.1>.
- FMI, 2016. Finish Meteorological Institute. <http://en.ilmatieteenlaitos.fi>.
- Gueymard, C.A., 2014. A review of validation methodologies and statistical performance indicators for modeled solar radiation data: towards a better bankability of solar projects. *Renew. Sustain. Energy Rev.* 39, 1024–1034. <https://doi.org/10.1016/j.rser.2014.07.117>.
- Gui, S., Liang, S., Wang, K., Li, L., Zhang, a.X., 2010. Assessment of three satellite-estimated land surface downwelling shortwave irradiance data sets. *Geosci. Rem. Sens. Lett. IEEE* 7 (4), 776–780. <https://doi.org/10.1109/LGRS.2010.2048196>.
- Hao, D., Asrar, G.R., Zeng, Y., Zhu, Q., Wen, J., Xiao, Q., Chen, M., 2020. DSCOVR/EPIC-derived global hourly and daily downward shortwave and photosynthetically active radiation data at $0.1^\circ \times 0.1^\circ$ resolution. *Earth Syst. Sci. Data* 12 (3), 2209–2221.
- Hatzianastassiou, N., Matsoukas, C., Fotiadi, A., Pavlakis, K.G., Drakakis, E., Hatzidimitriou, D., Vardavas, I., 2005. Global distribution of Earth's surface shortwave radiation budget. *Atmos. Chem. Phys.* 5, 2847–2867.
- Hinkelmann, L.M., Stackhouse Jr., P.W., Wielicki, B.A., Zhang, T., Wilson, S.R., 2009. Surface insolation trends from satellite and ground measurements: comparisons and challenges. *J. Geophys. Res.* 114 (D10).
- Huang, G., Li, Z., Li, X., Liang, S., Yang, K., Wang, D., Zhang, Y., 2019. Estimating surface solar irradiance from satellites: past, present, and future perspectives. *Rem. Sens. Environ.* 233, 111371. <https://doi.org/10.1016/j.rse.2019.111371>.

- Jia, B., Xie, Z., Dai, A., Shi, C., Chen, F., 2013. Evaluation of satellite and reanalysis products of downward surface solar radiation over East Asia: spatial and seasonal variations. *J. Geophys. Res.: Atmosphere* 118 (9), 3431–3446. <https://doi.org/10.1002/jgrd.50353>.
- Jiang, H., Lu, N., Qin, J., Tang, W., Yao, L., 2019. A deep learning algorithm to estimate hourly global solar radiation from geostationary satellite data. *Renew. Sustain. Energy Rev.* 114, 109327. <https://doi.org/10.1016/j.rser.2019.109327>.
- Kapsch, M.-L., Graversen, R.G., Tjernström, M., Bintanja, R., 2016. The effect of downwelling longwave and shortwave radiation on arctic summer sea ice. *J. Clim.* 29 (3), 1143–1159. <https://doi.org/10.1175/JCLI-D-15-0238.1>.
- Karlsson, K.-G., Anttila, K., Trentmann, J., Stengel, M., Fokke Meirink, J., Devasthale, A., Hanschmann, T., Kothe, S., Jääskeläinen, E., Sedlar, J., Benas, N., van Zadelhoff, G.-J., Schlundt, C., Stein, D., Finkensieper, S., Häkansson, N., Hollmann, R., 2017. CLARA-A2: the second edition of the CM SAF cloud and radiation data record from 34 years of global AVHRR data. *Atmos. Chem. Phys.* 17 (9), 5809–5828. <https://doi.org/10.5194/acp-17-5809-2017>.
- Karlsson, K.-G., Riihelä, A., Müller, R., Meirink, J.F., Sedlar, J., Stengel, M., Lockhoff, M., Trentmann, J., Kaspar, F., Hollmann, R., Wolters, E., 2013. CLARA-A1: a cloud, albedo, and radiation dataset from 28 yr of global AVHRR data. *Atmos. Chem. Phys.* 13 (10), 5351–5367. <https://doi.org/10.5194/acp-13-5351-2013>.
- Kato, S., Loeb, N.G., Doelling, D.R., Rose, F.G., Rutan, D.A., Caldwell, T.E., Yu, L., Weller, R.A., 2013. Surface irradiances consistent with CERES-derived top-of-atmosphere shortwave and longwave irradiances. *J. Clim.* 26 (9), 2719–2740. <https://doi.org/10.1175/JCLI-D-12-00436.1>.
- Liang, S., Cheng, J., Jia, K., Jiang, B., Liu, Q., Xiao, Z., Yao, Y., Yuan, W., Zhang, X., Zhao, X., 2021. The global Land surface satellite (GLASS) product suite. *Bull. Am. Meteorol. Soc.* 102 (2), E323–E337.
- Liang, S., Wang, D., He, T., Yu, Y., 2019. Remote sensing of earth's energy budget: synthesis and review. *International Journal of Digital Earth* 12 (7), 737–780. <https://doi.org/10.1080/17538947.2019.1597189>.
- Liang, S., Wang, K., Zhang, X., Wild, M., 2010. Review on estimation of land surface radiation and energy budgets from ground measurement, remote sensing and model simulations. *IEEE Journal of Selected Topics in Applied Earth Observations and Remote Sensing* 3 (3), 225–240. <https://doi.org/10.1109/JSTARS.2010.2048556>.
- Ma, H., Liang, S., Shi, H., Zhang, Y., 2020. An optimization approach for estimating multiple land surface and atmospheric variables from the geostationary advanced Himawari imager top-of-atmosphere observations. *IEEE Trans. Geosci. Rem. Sens.* 59 (4), 2888–2908.
- McMurdo Dry Valleys LTER, Doran, P., Fountain, A., 2019a. McMurdo Dry Valleys LTER: Daily Measurement Summaries from Canada Glacier Meteorological Station (CAAM) in Taylor Valley, Antarctica from 1994 to Present. <https://doi.org/10.6073/PASTA/6B40F960061394C157C89B111D963492>.
- McMurdo Dry Valleys LTER, Doran, P., Fountain, A., 2019b. McMurdo Dry Valleys LTER: Daily Measurement Summaries from Lake Bonney Meteorological Station (BOYM) in Taylor Valley, Antarctica from 1993 to Present. <https://doi.org/10.6073/PASTA/3220523D0AA8489375A9997856EC1A9>.
- McMurdo Dry Valleys LTER, Doran, P., Fountain, A., 2019c. McMurdo Dry Valleys LTER: Daily Measurement Summaries from Lake Fryxell Meteorological Station (FRLM) in Taylor Valley, Antarctica from 1993 to Present. <https://doi.org/10.6073/PASTA/1AC8DA354BF946F8C81B4EEC393737F0>.
- McMurdo Dry Valleys LTER, Doran, P., Fountain, A., 2019d. McMurdo Dry Valleys LTER: Daily Measurement Summaries from Lake Hoare Meteorological Station (HOEM) in Taylor Valley, Antarctica from 1987 to Present. <https://doi.org/10.6073/PASTA/BE2F27D49D9E0289FFD64871A6E1F3D1>.
- McMurdo Dry Valleys LTER, Doran, P., Fountain, A., 2019e. McMurdo Dry Valleys LTER: Daily Measurement Summaries from Lake Vida Meteorological Station (VIAM) in Victoria Valley, Antarctica from 1995 to Present. <https://doi.org/10.6073/PASTA/8864645B519274A28F6F94D9619A2958>.
- McMurdo Dry Valleys LTER, Doran, P., Fountain, A., 2019f. McMurdo Dry Valleys LTER: Daily Measurement Summaries from Miers Valley Meteorological Station (MISM) in Miers Valley, Antarctica from 2012 to Present. <https://doi.org/10.6073/PASTA/65234DF2904F948F1EBCEBF12CB27D09>.
- McMurdo Dry Valleys LTER, Doran, P., Fountain, A., 2019g. McMurdo Dry Valleys LTER: daily measurement summaries from taylor glacier meteorological station (TARM) in taylor valley, Antarctica from 1994 to present. <https://doi.org/10.6073/PASTA/F0F586D88BEEF27032CEF66C0BC363B>.
- Mueller, R.W., Matsoukas, C., Gratzki, A., Behr, H.D., Hollmann, R., 2009. The CM-SAF operational scheme for the satellite based retrieval of solar surface irradiance — a LUT based eigenvector hybrid approach. *Rem. Sens. Environ.* 113 (5), 1012–1024. <https://doi.org/10.1016/j.rse.2009.01.012>.
- Muneer, T., Younes, S., Munawarw, S., 2007. Discourses on solar radiation modeling: AS. Renew. Sustain. Energy Rev. 11 (4), 551–602. <https://doi.org/10.1016/j.rser.2005.05.006>.
- NIBIO-LMT, 2016. Norwegian Institute of Bioeconomy Research) - Landbruksmeteorologisk Tjeneste. <http://lmt.nibio.no/>.
- Pastorello, G., Trotta, C., Canfora, E., Chu, H., Christianson, D., Cheah, Y.-W., Poindexter, C., Chen, J., Elbshandy, A., Humphrey, M., Isaac, P., Polidori, D., Reichstein, M., Ribeca, A., van Ingen, C., Vuichard, N., Zhang, L., Amiro, B., Ammann, C., Papale, D., 2020. The FLUXNET2015 dataset and the ONEFlux processing pipeline for eddy covariance data. *Scientific Data* 7 (1), 225. <https://doi.org/10.1038/s41597-020-0534-3>.
- Pfeifroth, U., Sanchez-Lorenzo, A., Manara, V., Trentmann, J., Hollmann, R., 2018. Trends and variability of surface solar radiation in Europe based on surface- and satellite-based data records. *J. Geophys. Res.: Atmosphere* 123 (3), 1735–1754. <https://doi.org/10.1002/2017JD027418>.
- Pinker, R.T., Laszlo, I., 1992. Modeling surface solar irradiance for satellite applications on a global scale: GEWEB. *J. Appl. Meteorol.* 31 (2), 194–211. [https://doi.org/10.1175/1520-0450\(1992\)031<0194:MSSIFS>2.0.CO;2](https://doi.org/10.1175/1520-0450(1992)031<0194:MSSIFS>2.0.CO;2).
- Posselt, R., Mueller, R.W., Stöckli, R., Trentmann, J., 2012. Remote sensing of solar surface radiation for climate monitoring — the CM-SAF retrieval in international comparison. *Rem. Sens. Environ.* 118, 186–198. <https://doi.org/10.1016/j.rse.2011.11.016>.
- Riihelä, A., Key, J.R., Meirink, J.F., Kuipers Munneke, P., Palo, T., Karlsson, K.-G., 2017. An intercomparison and validation of satellite-based surface radiative energy flux estimates over the Arctic. *J. Geophys. Res.: Atmosphere* 122 (9), 4829–4848. <https://doi.org/10.1002/2016JD026443>.
- Roesch, A., Wild, M., Ohmura, A., Dutton, E.G., Long, C.N., Zhang, T., 2011. Assessment of BSRN radiation records for the computation of monthly means: BSRN. *Atmospheric Measurement Techniques* 4 (2), 339–354. <https://doi.org/10.5194/amt-4-339-2011>.
- Rutan, D.A., Kato, S., Doelling, D.R., Rose, F.G., Le Nguyen, T., Caldwell, T.E., Loeb, N.G., 2015. CERES synoptic product: methodology and validation of surface radiant flux: CERES1. *J. Atmos. Ocean. Technol.* 32 (6), 1121–1143. <https://doi.org/10.1175/JTECH-D-14-00165.1>.
- Ryu, Y., Jiang, C., Kobayashi, H., Detto, M., 2018. MODIS-derived global land products of shortwave radiation and diffuse and total photosynthetically active radiation at 5 km resolution from 2000. *Rem. Sens. Environ.* 204, 812–825.
- Sanchez-Lorenzo, A., Wild, M., Brunetti, M., Guijarro, J.A., Hakuba, M.Z., Calbó, J., Mistakidis, S., Bartok, B., 2015. Reassessment and update of long-term trends in downward surface shortwave radiation over Europe (1939–2012). *J. Geophys. Res.: Atmosphere* 120 (18), 9555–9569. <https://doi.org/10.1002/2015JD023321>.
- Steffen, K., Box, J.E., Abdalati, W., 1996. Greenland climate network: GC-Net. *US Army Cold Regions Reattach and Engineering (CRREL), CRREL Special Report 98-103*.
- Stephens, G.L., Li, J., Wild, M., Clayton, C.A., Loeb, N., Kato, S., L'Ecuyer, T., Stackhouse, P.W., Lebsack, M., Andrews, T., 2012. An update on Earth's energy balance in light of the latest global observations. *Nat. Geosci.* 5 (10), 691–696. <https://doi.org/10.1038/ngeo1580>.
- Sun, D., Ji, C., Sun, W., Yang, Y., Wang, H., 2018. Accuracy assessment of three remote sensing shortwave radiation products in the Arctic: Arctic. *Atmos. Res.* 212, 296–308. <https://doi.org/10.1016/j.atmosres.2018.01.003>.
- U.S. National Ice Center, 2008. IMS Daily Northern Hemisphere Snow and Ice Analysis at 1 Km, 4 Km, and 24 Km Resolutions. NSIDC: National Snow and Ice Data Center, Boulder, Colorado USA. <https://doi.org/10.7265/N52R3PMC>. Version 1.
- Urraca, R., Gracia-Amillo, A.M., Koublí, E., Huld, T., Trentmann, J., Riihelä, A., Lindfors, A.V., Palmer, D., Gottschalg, R., Antonanzas-Torres, F., 2017. Extensive validation of CM-SAF surface radiation products over Europe. *Rem. Sens. Environ.* 199, 171–186. <https://doi.org/10.1016/j.rse.2017.07.013>.
- Wang, D., 2017. MODIS/Terra+Aqua Surface Radiation Daily/3-Hour L3 Global 5km SIN Grid V006. <https://doi.org/10.5067/MODIS/MCD18A1.006>.
- Wang, D., 2021. MODIS/Terra+Aqua Surface Radiation Daily/3-Hour L3 Global 1km SIN Grid V061. <https://doi.org/10.5067/MODIS/MCD18A1.061>.
- Wang, D., Liang, S., 2014. Improving LAI mapping by integrating MODIS and CYCLOPES LAI products using optimal interpolation. *IEEE Journal of Selected Topics in Applied Earth Observations and Remote Sensing* 7 (2), 445–457. <https://doi.org/10.1109/jstas.2013.2264870>.
- Wang, D., Liang, S., He, T., Shi, Q., 2015. Estimation of daily surface shortwave net radiation from the combined MODIS data. *IEEE Trans. Geosci. Rem. Sens.* 53 (10), 5519–5529.
- Wang, D., Liang, S., Zhang, Y., Gao, X., Brown, M.G.L., Jia, A., 2020. A new set of MODIS land products (MCD18): downward shortwave radiation and photosynthetically active radiation. *Rem. Sens.* 12 (1), 168. <https://doi.org/10.3390/rs12010168>.
- Wang, D., Morton, D., Masek, J., Wu, A., Nagol, J., Xiong, X., Levy, R., Vermote, E., Wolfe, R., 2012. Impact of sensor degradation on the MODIS NDVI time series. *Rem. Sens. Environ.* 119, 55–61. <https://doi.org/10.1016/j.rse.2011.12.001>.
- Wang, T., Yan, G., Chen, L., 2012. Consistent retrieval methods to estimate land surface shortwave and longwave radiative flux components under clear-sky conditions. *Rem. Sens. Environ.* 124, 61–71.
- Wild, M., Trüssel, B., Ohmura, A., Long, C.N., König-Langlo, G., Dutton, E.G., Tsvetkov, A., 2009. Global dimming and brightening: an update beyond 2000. *J. Geophys. Res.: Atmosphere* 114 (D10).
- Wu, F., Fu, C., 2011. Assessment of GEWEX/SRB version 3.0 monthly global radiation dataset over China. *Meteorol. Atmos. Phys.* 112 (3–4), 155–166. <https://doi.org/10.1007/s00703-011-0136-x>.
- Xia, X.A., Wang, P.C., Chen, H.B., Liang, F., 2006. Analysis of downwelling surface solar radiation in China from National Centers for Environmental Prediction reanalysis, satellite estimates, and surface observations. *J. Geophys. Res.* 111 (D9), L06803. <https://doi.org/10.1029/2005JD006405>.
- Yu, Y., Shi, J., Wang, T., Letu, H., Yuan, P., Zhou, W., Hu, L., 2019. Evaluation of the himawari-8 shortwave downward radiation (SWDR) product and its comparison with the CERES-SYN, MERRA-2, and ERA-interim datasets. *IEEE Journal of Selected Topics in Applied Earth Observations and Remote Sensing* 12 (2), 519–532. <https://doi.org/10.1109/JSTARS.2018.2851965>.
- Yu, Y., Wang, T., Shi, J. (Eds.), 2018. Assessment of Two Satellite-Based Land Surface Shortwave Downward Radiation Datasets over the Tibetan Plateau. IEEE.
- Zhang, T., Stackhouse, P.W., Gupta, S.K., Cox, S.J., Colleen Mikovitz, J., Hinkelmann, L.M., 2013. The validation of the GEWEX SRB surface shortwave flux data products using BSRN measurements: a systematic quality control, production and application approach. *J. Quant. Spectrosc. Radiat. Transf.* 122, 127–140. <https://doi.org/10.1016/j.jqsrt.2012.10.004>.
- Zhang, X., Liang, S., Wang, G., Yao, Y., Jiang, B., Cheng, J., 2016. Evaluation of the reanalysis surface incident shortwave radiation products from NCEP, ECMWF, GSFC,

- and JMA using satellite and surface observations. *Rem. Sens.* 8 (3), 225. <https://doi.org/10.3390/rs8030225>.
- Zhang, X., Liang, S., Wild, M., Jiang, B., 2015. Analysis of surface incident shortwave radiation from four satellite products. *Rem. Sens. Environ.* 165, 186–202. <https://doi.org/10.1016/j.rse.2015.05.015>.
- Zhang, X., Liang, S., Zhou, G., Wu, H., Zhao, X., 2014. Generating Global LAnd Surface Satellite incident shortwave radiation and photosynthetically active radiation products from multiple satellite data. *Rem. Sens. Environ.* 152, 318–332. <https://doi.org/10.1016/j.rse.2014.07.003>.
- Zhang, X., Zhao, X., Li, W., Liang, S., Wang, D., Liu, Q., Yao, Y., Jia, K., He, T., Jiang, B., Wei, Y., Ma, H., 2019. An operational approach for generating the global land surface downward shortwave radiation product from MODIS data. *IEEE Trans. Geosci. Rem. Sens.* 57 (7), 4636–4650. <https://doi.org/10.1109/TGRS.2019.2891945>.
- Zhang, Y. [Yehui], Seidel, D.J., Golaz, J.-C., Deser, C., Tomas, R.A., 2011. Climatological characteristics of Arctic and Antarctic surface-based inversions. *J. Clim.* 24 (19), 5167–5186.
- Zhang, Y. [Yuanchong], Rossow, W.B., Lacis, A.A., Oinas, V., Mishchenko, M.I., 2004. Calculation of radiative fluxes from the surface to top of atmosphere based on ISCCP and other global data sets: refinements of the radiative transfer model and the input data: isccp. *J. Geophys. Res.* 109 (D19) <https://doi.org/10.1029/2003JD004457>.
- Zhang, Y. [Yil], Liang, S., He, T., Wang, D., Yu, Y., Ma, H., 2020. Estimation of land surface incident shortwave radiation from geostationary advanced Himawari imager and advanced baseline imager observations using an optimization method. *IEEE Trans. Geosci. Rem. Sens.*